
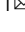


## Unambiguous joint detection of spatially separated properties of a single photon in the two arms of an interferometer

Surya Narayan Sahoo<sup>1</sup>, Sanchari Chakraborti<sup>1</sup>, Som Kanjilal<sup>2</sup>, Saumya Ranjan Behera<sup>1</sup>, Dipankar Home<sup>2</sup>, Alex Matzkin<sup>3</sup> & Urbasi Sinha<sup>1</sup>  

The quantum superposition principle implies that a particle entering an interferometer evolves by simultaneously taking both arms. If a non-destructive, minimally-disturbing interaction coupling a particle property to a pointer is implemented on each arm while maintaining the path superposition, quantum theory predicts that, for a fixed state measured at the output port, certain particle properties can be associated with only one or the other path. This phenomenon is known as the quantum Cheshire cat effect. Here we report the realization of this prediction through joint observation of the spatial and polarization degrees of freedom of a single photon in the two respective arms of an interferometer. Significant pointer shifts ( $\sim 50$  microns), corresponding to measured weak values, are observed in each arm. This observation, involving coupling distinct properties of a quantum system in spatially separated regions, opens new possibilities for quantum information protocols and for tests of quantumness for mesoscopic systems.

<sup>1</sup>Light and Matter Physics, Raman Research Institute, Bengaluru 560080, India. <sup>2</sup>Center for Astroparticle Physics and Space Science (CAPSS), Bose Institute, Kolkata 700 091, India. <sup>3</sup>Laboratoire de Physique Théorique et Modélisation, CNRS Unité 8089, CY Cergy Paris Université, 95302 Cergy-Pontoise cedex, France. ✉email: [usinha@rri.res.in](mailto:usinha@rri.res.in)

A quantum particle, say a single photon entering an interferometer, is said to travel along both arms simultaneously<sup>1</sup>. This is generally evidenced by monitoring the resulting interference at the exit port. Instead, if a measurement is made earlier on one or the other arm, the photon will be detected on that arm with some probability, and the interference pattern will disappear. Modifying an interaction at an intermediate time, such as removing the exit beam-splitter once the photon is already inside the interferometer in the famous delayed-choice experiment<sup>2</sup>, changes the observed properties of the photon.

These manifestations of the quantum superposition of states open avenues for empirically probing other intriguing questions, such as whether it is possible to jointly detect signatures of distinct particle properties in different arms of an interferometer. Such joint detections hinge on the implementation of non-destructive measurements on both arms while maintaining the coherence of the particle throughout its evolution. In this work, we will present experimental results obtained by implementing a form of minimally perturbing non-destructive measurements known as weak measurements<sup>3</sup>. We will be interested in the particular case in which a given property can be detected in only one of the arms, while a different property of the same particle can be detected only in the other arm. This is an instance of the scenario proposed some time ago, which was coined the “Quantum Cheshire Cat” (QCC) effect<sup>4</sup>. Earlier experiments<sup>5–8</sup> have not been able to observe the Quantum Cheshire Cat effect in terms of the joint detection of spatially separated distinct properties of the same particle in the respective two arms. For this purpose, it is necessary to perform joint weak measurements of two different properties in the two arms by ensuring there is only one particle within the setup during each run of the experiment—a key requirement that has not yet been realized in any experiment to date<sup>9</sup>. In this work, we demonstrate the first, to the best of our knowledge, direct measurement of the weak values of different observables of a single quantum particle in separate spatial regions. By using quantum pointers along both arms of a Mach–Zehnder interferometer, we detect jointly the effect of coupling the photon’s spatial DOF on one arm and coupling the diagonal polarization DOF on the other arm by showing shifts of ~50 microns in the corresponding pointer position.

## Results

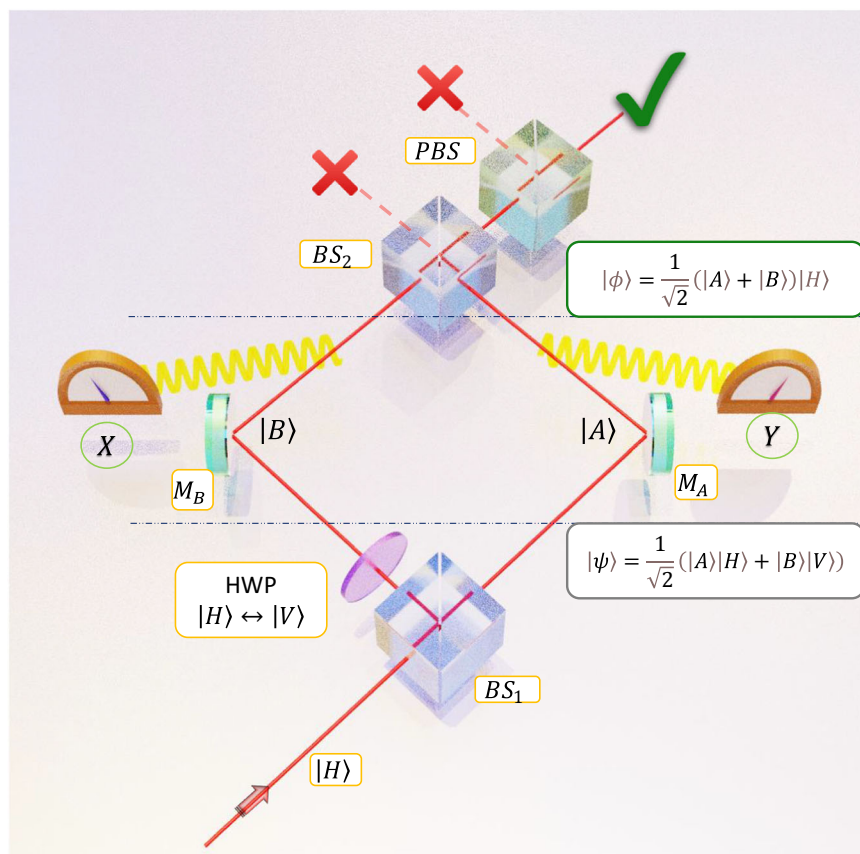
**General scheme.** Consider a single photon entering the Mach–Zehnder interferometer (MZI) of Fig. 1. We prepare the state after the beam-splitter  $BS_1$  to be  $|\psi\rangle = \frac{1}{\sqrt{2}}(|A\rangle|H\rangle + |B\rangle|V\rangle)$ , where  $|A\rangle$  and  $|B\rangle$  denote the spatial wavefunctions in arms A and B respectively; this preparation procedure is known as “pre-selection”<sup>10</sup>. When detecting the photon at the exit port, we filter the measured state keeping only the outcomes corresponding to  $|\phi\rangle = \frac{1}{\sqrt{2}}(|A\rangle + |B\rangle)|H\rangle$ . This filtering procedure is known as “post-selection”. Let  $\hat{Y}_i = |i\rangle\langle i| \otimes \hat{\mathbb{1}}$  represent the spatial projection operator on arm  $i = A, B$  and let  $\hat{X}_i = |i\rangle\langle i| \otimes \hat{\sigma}_1$  represent a diagonal polarization measurement operator on arm  $i$  ( $\hat{\sigma}_1$  is a Pauli matrix). The probability for the photon to be found on arm A (conditioned on successful post-selection of  $|\phi\rangle$ ) is given by  $P(Y_A = 1|\phi) = 1$ <sup>11</sup>, and therefore on arm B  $P(Y_B = 1|\phi) = 0$  ( $Y_i = 0, 1$  denotes the eigenvalues of  $\hat{Y}_i$ ): a non-destructive intermediate projective measurement of the position degree of freedom will always find the photon on arm A, as detailed in Supplementary Note 1. However, if the polarization of the photon in the diagonal basis  $\{| \nearrow \rangle, | \searrow \rangle\}$  on a particular path  $i$  i.e.,  $\hat{X}_i$  is measured, instead of the position, there is a non-zero probability of finding a photon on arm B with diagonal  $| \nearrow \rangle$  or anti-diagonal

$| \searrow \rangle$  polarization (see Section 1.3 of Supplementary Note 1). There is, nevertheless, no paradox: Bohr<sup>12</sup> and Wheeler<sup>13</sup> proscribed long ago the use of counterfactual reasoning while attempting to account for the behavior of quantum systems measured under different experimental conditions within a single picture. If only  $\hat{X}_B$  is measured, one can not ascribe a property to the spatial position of the same photon on arm A had  $\hat{Y}_A$  been measured. When  $\{\hat{X}_B, \hat{Y}_A\}$  are measured jointly, the system coherence is disturbed, and we will obtain with equal probabilities either the photon position on arm A or the photon’s diagonal polarization on arm B (see Section 1.4 of Supplementary Note 1).

In order to keep the coherence essentially intact while jointly detecting the spatially separated properties on each arm for a single photon in the same run of the experiment, minimally disturbing intermediate interactions need to be implemented. This is the objective of our experiment. For this purpose, we use what are known as weak measurements<sup>3</sup>, wherein very weak couplings are combined with pre and post-selected states (as defined in Fig. 1). In this situation, the shift of a pointer weakly coupled to a system observable  $\hat{S}$  is proportional to the real part of a quantity known as the weak value  $S^w = \langle \phi | \hat{S} | \psi \rangle / \langle \phi | \psi \rangle$  (see Section 2.1 of Supplementary Note 2). In the present setup, with the notation, introduced previously, it follows that  $Y_A^w = 1, X_B^w = 1$  (see Section 2.2 of Supplementary Note 2). These weak values imply the following key feature: the pointer that is weakly coupled to  $Y_A$ , the spatial degrees of freedom (DOF) on arm A, and the pointer that is weakly coupled to the diagonal polarization DOF on arm B ( $X_B$ ) both shift when a single photon passes through the interferometer. In addition, a logical consequence of having these weak values equal to unity is that  $Y_B^w = 0$  and  $X_A^w = 0$  (the proof is given in Supp. Info. 2), so that weakly coupling the spatial DOF on arm B or the diagonal polarization DOF on arm A has no effect on the respective pointers. Thus, the pointers’ motions resulting from the weak couplings can be interpreted as reflecting the ‘superposition’ of these two different photon properties along spatially separated arms. This spatial separation of the position degree of freedom from another property is an instance of the “Quantum Cheshire Cat”<sup>1</sup>.

Genuine weak measurements are generally delicate to implement experimentally, given that the coupling is weak and the experimentally measured quantities are often of the same order of magnitude as the experimental errors for certain choices of pre- and post-selection. Several experiments in the last 15 years have measured weak values and their ramifications<sup>14–20</sup>. Very often, however, weak values are inferred by combining distinct projective (strong coupling) measurements. This has been the case, particularly for past interferometric experiments<sup>5–8,21</sup> attempting to observe the QCC effect.

**Experimental setup.** In order to jointly observe the spatially separated properties in an interferometer, it is crucial to implement non-destructive minimally perturbing measurements on the same quantum particle. While sequential weak measurements on the same particle have been performed in the past<sup>22,23</sup>, in this work, we need to implement joint weak measurements on the same particle along both arms, that is in distinct locations. More specifically, employing the experimental architecture shown in Fig. 2 with a single photon source, we perform joint weak measurements of  $\hat{Y}_A$ , the spatial DOF of the photon in arm A, and of  $\hat{X}_B$ , the diagonal component of polarization DOF in arm B, in the same run of the experiment i.e. without any change in experimental settings between pre and post-selection. The photon is prepared in the pre-selected state  $|\psi\rangle$  and weakly interacts with the optical elements associated with the observables to be measured inside the interferometer. The center of the transverse



**Fig. 1 Schematics of a Mach-Zehnder interferometer with pre- and post-selection.** The observables  $\hat{X}$  and  $\hat{Y}$  are coupled to the pointers at an intermediate time between pre-selection with state  $|\psi\rangle$  and post-selection with state  $|\phi\rangle$ . In the figure, PBS, BS, and HWP stand for polarizing beam splitter, beam splitter, and half-wave plate, respectively.

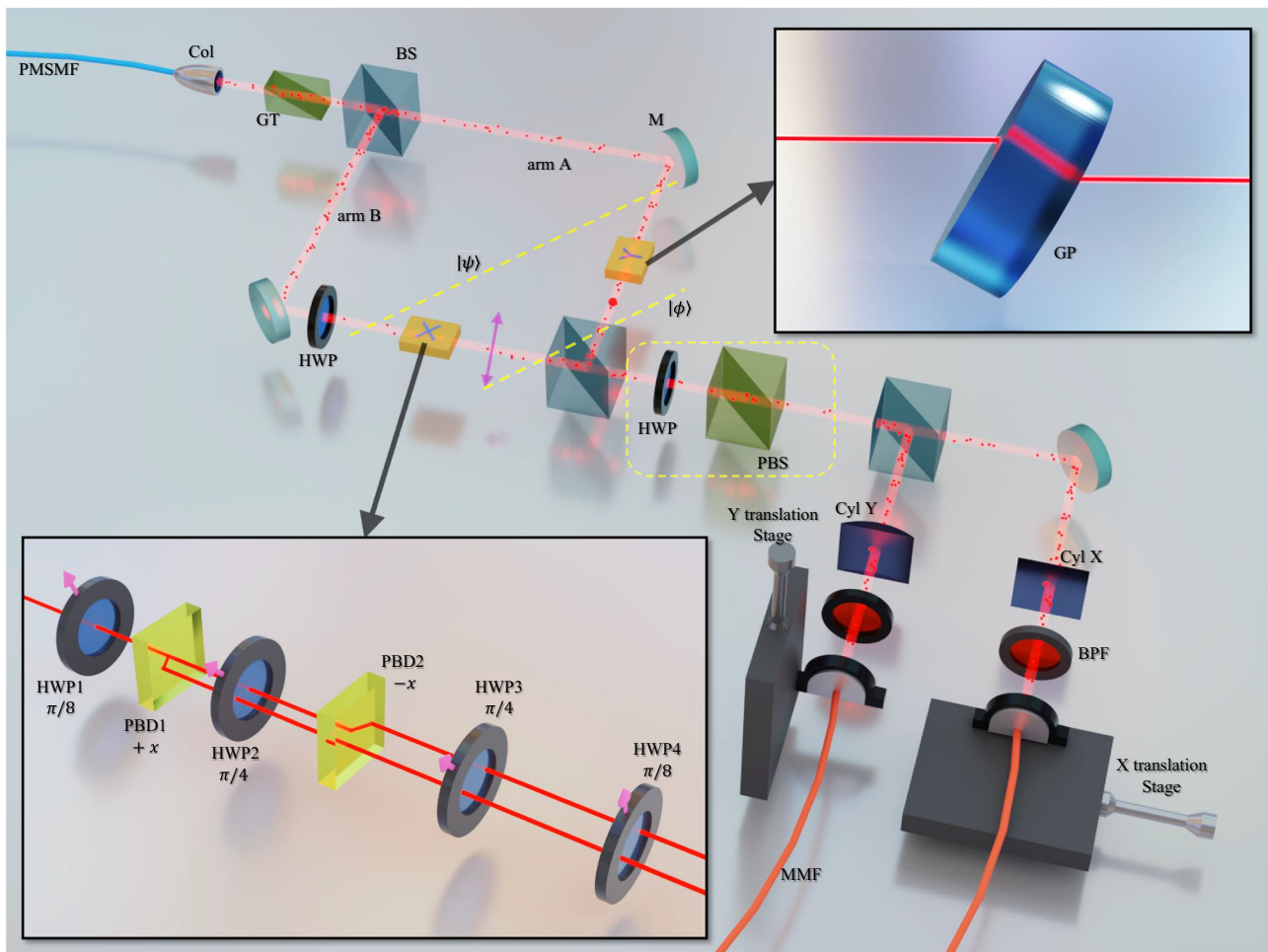
spatial profile (approximately Gaussian) of the beam is chosen as the pointer position. For the interaction involving the spatial DOF (i.e., for  $\hat{Y}_A$ ), we use a tilted glass plate that causes a vertical shift of the overall beam. The coupling of  $\hat{X}_B$  is made with a combination of several HWPs and two beam displacers that cause a horizontal shift in the pointer after the post-selection. A polarizing beam-splitter at the output port post-selects the photon to the state  $|\phi\rangle$ . Finally, the weak values are inferred by measuring the horizontal and vertical shifts of the pointer (i.e., from the center of the transverse profile of the beam). Each step of the experiment is detailed in the Methods.

Being an interferometric experiment, steps have been taken to ensure maximum coherence as well as proper phase stabilization. One of the key features that we need to ensure in order to enable an unambiguous joint measurement is a perfect overlap of the beams from the individual arms in the absence of the desired weak interaction. This involves a critical alignment procedure involving measuring the undeviated beam positions while including all necessary interaction components. We also need to ascertain the values of the exact pointer shifts in microns for both the weak interactions that would correspond to a weak value of 1, requiring further calibration (see Methods). Ensuring coherence and maximum visibility requires prior alignment with a pulsed laser and a beam profiler camera before moving on to the heralded photon source.

A crucial requirement in our experiment is to ensure that we are performing joint measurements on the same photon. The use of heralded photons in our experiment ensures the same. We use a photon source based on the process of spontaneous parametric down-conversion (SPDC). The SPDC process leads to the

production of two photons of lower energy for an incident pump photon. Thus SPDC is a twin-photon source. In order to ensure that we deal with one and only one photon in an experimental run, we use the process of heralding. This essentially means detecting one of the photons (conventionally referred to as the idler photon) and using this detection as proof of the existence of the other photon in the pair (conventionally referred to as the signal photon), in other words detecting one photon heralds the presence of the other. As both photons are produced at the same time, in principle, they also reach their individual detectors at the same time. Thus measuring an intensity-intensity correlation function between the two detectors gives us what is called the “coincidence” value. The number of coincidences indicates the number of occurrences of the twin-photon event. This then also gives us the number of single photons corresponding to its coincident partner photon. In our experiment, the signal photon passes through the interferometric set-up while the photon in the heralding arm is used to enable the measurement of coincidences at the desired pre- and post-selection conditions. We also show a measurement of cross-correlation ( $g_2$  measurement) in the Methods section to further substantiate the fulfillment of the one photon at a time requirement.

**Measurement of weak values.** We show a representative result from our experiment in Fig. 3. The figure demonstrates the histogram of weak values obtained for  $X^w$  (a component of polarization DOF) and  $Y^w$  (spatial DOF) measured jointly for the prepared pre-selected state  $|\psi\rangle$  and post selected state  $|\phi\rangle$  given above. Experimentally we reconstruct the transverse profile of the beam along the horizontal (X) and vertical (Y) directions by



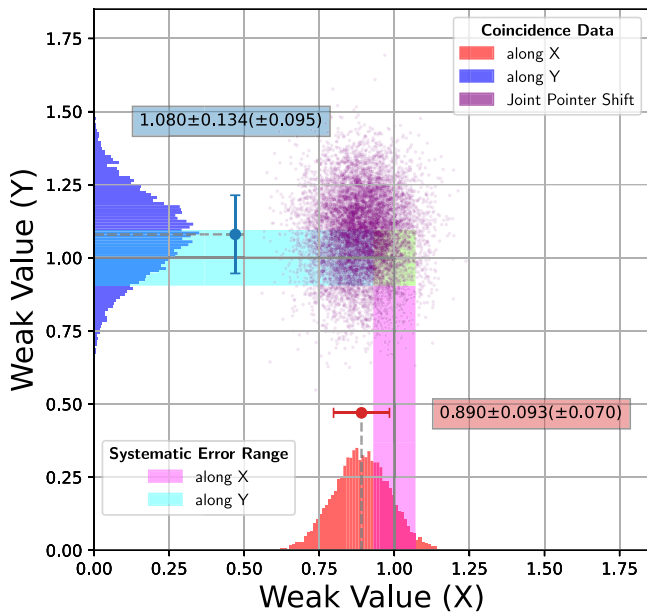
**Fig. 2 Simplified experimental setup showing the Mach-Zehnder interferometer (MZI) with pre and post-selection.** The angle of the post-selection Half-Wave Plate (HWP) is kept at zero degrees to get the desired post-selection  $|\phi\rangle$ . In arm B, the apparatus to measure the  $\sigma_x$  polarization component is inserted, which displaces the beam along the horizontal (along X). The glass plate (GP) in arm A makes the beam shift vertically (along Y). A 50:50 beam splitter placed after the post-selecting Polarizing Beam Splitter (PBS) causes the photons to randomly make their way to either of the two multi-mode fibers (MMF). One of the fibers is moved along X to generate the horizontal profile of the beam after the beam passes through a cylindrical lens that compresses the vertical transverse profile. The other MMF is moved along Y to generate the vertical profile of the beam after the horizontal transverse profile of the beam is compressed using another cylindrical lens. The two weak interactions in the respective arms occur at the same time and no experimental setting is changed between pre- and post-selection during the data acquisition. The coincidence measurement ensures that there is almost always a single photon within the interferometer interacting with the two operators ( $\hat{X}$  and  $\hat{Y}$ ) in the two respective arms of the interferometer simultaneously.

collecting photon statistics at different positions, along the particular direction, using the respective multi-mode fibers as mentioned in Fig. 2 and measuring the pointer shifts associated with the two interactions  $\hat{X}_B$  and  $\hat{Y}_A$  from the positions of the centers of the respective profiles. From  $10^4$  such profile reconstructions we obtain the pointer shift along X to be  $53.468 \pm 5.592 \mu\text{m}$  and the pointer shift along Y to be  $56.809 \pm 7.026 \mu\text{m}$ , where the values represent the mean  $\pm 1\sigma$  error respectively. The weak values are then evaluated from the respective pointer shifts; we obtain  $X^w$  to be  $0.89 \pm 0.09$  and  $Y^w$  to be  $1.08 \pm 0.13$ , respectively, along with attendant systematic error bands as shown in Fig. 3. The systematic error range estimates the drift in scale with respect to which of the weak values is computed. This is primarily caused by beam-pointing fluctuations as well as the drift in the center of the beam due to the acoustic and thermal response of the optomechanical components.

Note that for technical reasons (see the Methods section), the MMFs employed to detect the photon cannot be moved diagonally. This is why the photon positions are shown in the

(X,Y) plane in Fig. 3 are obtained indirectly by extracting the horizontal and vertical components of the diagonal beam displacement by employing a detection scheme with a beamsplitter. The beamsplitter placed after the post-selecting PBS (see Fig. 2) sends the outgoing photon towards the MMF moved horizontally and the MMF moved vertically. The photon registration on either the horizontally (X) or the vertically (Y) translated MMF is random, thereby ensuring that the overall position of the photon is indeed displaced along both the X and Y directions.

To validate that the experimental results  $X^w$  and  $Y^w$  are indeed the weak values inferred from the pointer shifts obtained for the weak measurements of the observables  $\hat{X}$  and  $\hat{Y}$  respectively, the post-selection is varied by rotating a half-wave plate (HWP) placed just before the post-selecting PBS. This makes the post-selected state to be  $|\phi(\theta)\rangle = \frac{1}{\sqrt{2}}(|A\rangle + |B\rangle) \otimes S(\theta)|H\rangle$ , where  $S(\theta)$  is the Jones matrix for the HWP with its fast axis oriented at  $\theta$  with reference to the horizontal. The observed pointer shifts along X for several post-selection states along with the theoretical curve for the weak value of the diagonal spin component are shown in



**Fig. 3 Measured weak values of the diagonal polarization (X) and spatial (Y) degrees of freedom.** The coincidence distribution (photon detected in coincidence with the corresponding heralded photon) of the photons for  $X^w$  is shown on the X axis through the red histogram plot. The mean and  $1\sigma$  errors from the distribution are shown above the histogram while the values are mentioned alongside the box. Similarly, the distribution for  $Y^w$  is shown along the Y-axis through the blue histogram plot. Since both the pointer shifts occur concurrently and are measured jointly in the experiment (i.e., without changing anything between pre and post-selection), the overall shift of the pointer is along the diagonal, as inferred from the shifts on the projections along horizontal X and vertical Y. The distribution of these diagonal shifts, in terms of the weak values, is represented by the scatter plots. The pink and light blue bands represent the systematic error bands for the coincidence measurements ( $\pm 0.070$  for  $X^w$  and  $\pm 0.095$  for  $Y^w$ , respectively). As can be seen, both measured weak values ( $0.890 \pm 0.093$ ) for  $X^w$  (the diagonal component of the polarization DOF) and ( $1.080 \pm 0.134$ ) for  $Y^w$  (the spatial DOF) lie well within the systematic error band of the experiment. Details of the error analysis are given in the Methods section.

**Fig. 4a.** The measured pointer shifts along Y for the same post-selection angles are shown in Fig. 4b along with the corresponding weak value curve for the spatial projector.

The weak values  $X^w$  and  $Y^w$  are evaluated from the respective pointer shifts (X and Y) measured at a given post-selection angle  $\theta$  using the pointer shifts measured at two reference post-selection angles  $\theta = 45^\circ$  and  $\theta = 90^\circ$  corresponding to weak values of 0 and 1 respectively. For instance, for  $\theta = 0^\circ$ , the weak values for post-selection  $|\phi\rangle = |\phi(0^\circ)\rangle$  are computed as follows:

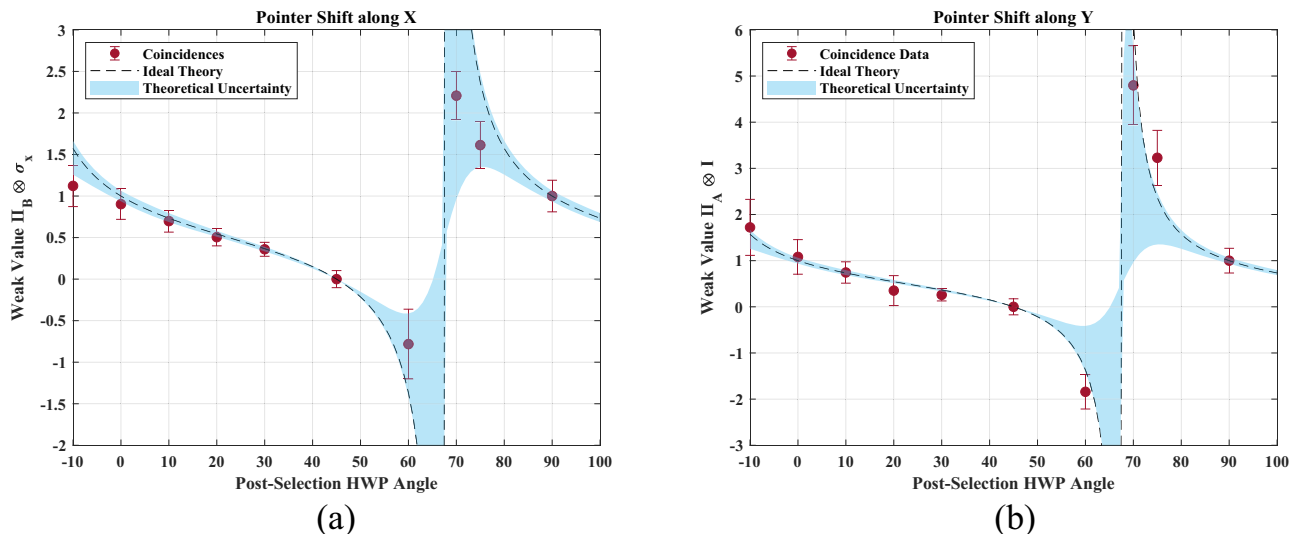
$$X^w = \frac{X - X_0}{\langle X_1 - X_0 \rangle}, \quad Y^w = \frac{Y - Y_0}{\langle Y_1 - Y_0 \rangle}$$

where  $(X_0, Y_0)$  and  $(X_1, Y_1)$  are the distribution of the pointer variables, i.e., the horizontal and vertical position of the beam center associated with  $10^4$  profiles reconstructed for post-selected states  $|\phi(45^\circ)\rangle$  and  $|\phi(90^\circ)\rangle$  respectively. The same method is used to calculate the weak values for X (the diagonal polarization component DOF) and Y (the spatial DOF) at other post-selection angles as well. Details of our data acquisition statistics, as well as detailed error analysis (both statistical as well as systematic errors), are discussed in the Methods section.

**Discussion**

These results are, to our knowledge, the first direct joint measurement of the weak values of different observables of a single quantum particle in distinct spatial regions. We have experimentally shown that a quantum pointer on one arm of the interferometer detects the spatial DOF of a photon in the chosen pre and post-selected states; at the same time, a pointer in the other arm detects the diagonal component of polarization DOF of the same photon. Our results should be contrasted with earlier experiments<sup>5-8,21</sup> in which the QCC effect was investigated indirectly through the combination of indirect measurements. The first experiment<sup>5</sup> measured matter-wave intensities in a neutron interferometer employing several distinct setups: to infer the presence of the neutron’s spatial degree of freedom on one arm, an absorber was placed in either arm, and the resulting intensity in each case was monitored. Similarly, in order to infer the spin component, a magnetic field applied in either arm rotates the spin, and the effect of the magnetic field on the intensity was monitored. It turns out that weak values can be reconstructed by combining intensities obtained from these different setups, but such an indirect method precludes the observation of spatially separated degrees of freedom of the same neutron<sup>9</sup>. A similar single photon experiment measuring photon counts in setups with or without absorbers and half-wave plates (inducing polarization rotations) alternatively placed on either arm was later realized<sup>7</sup>. More recently, in another single photon experiment<sup>8</sup>, weak values were obtained by interpolating experimental results obtained by coupling a photon pointer with different coupling strengths. Although the photon pointer might have promising applications, it was possible to couple such a pointer to the photon in only one arm. Moreover, independent runs with different coupling strengths were needed in order to interpolate values in the weak coupling regime. Hence this experiment, too, could not implement joint weak measurements and achieve the observation of different properties in the same run on the same photon<sup>24</sup>. Another experiment<sup>21</sup> using the QCC effect to demonstrate polarization exchange between entangled photons also employed a combination of indirect intensity measurements obtained from different setups so as to infer the weak values.

Our approach could pave the way to develop technologies implementing distinct interactions with different degrees of freedom of the same quantum system in different spatial regions, with minimal mutual perturbations. It should be worth exploring the application of the techniques used in our photonic experiment for demonstrating similar effects in massive particles by relying on the currently developing coherent atom-chip Stern-Gerlach interferometry<sup>25</sup> and thereby demonstrating an effect similar to the one shown in our photonic experiment. This could provide a potentially interesting dimension to the studies aiming to test the applicability of fundamental quantum features related to this work in the macroscopic regime. Our scheme could also be applied to quantum information protocols, for instance, to share the state of a qubit among spatially separated parties that would each couple an ancilla to the qubit. A procedure for counterfactual quantum communication based on the Quantum Cheshire Cat effect was proposed very recently<sup>26</sup>. Finally, we would like to conclude by raising the following provocative question: by going beyond Bohr’s dictum<sup>27</sup> that we have no right to speak about what a photon does within an interferometer, can the effect shown in our experiment be interpreted as refining Bohr’s principle of wave-particle complementarity? This is motivated by noting that in this experiment, the observables corresponding to particle-like properties of a single photon in each arm of the interferometer seemingly exhibit a wave-like superposition inside the interferometer. Of course, such a question needs to be



**Fig. 4** Weak values with varying post-selection angle. **a** Pointer shift along X (diagonal polarization component) as a function of post-selection angle with  $1\sigma$  error bar, **b** Pointer shift along Y (due to coupling the spatial degree of freedom) as a function of post-selection angle with  $1\sigma$  error bar. Only the photons detected in coincidence with the heralded photon are counted. The black dashed line in each plot represents the ideal theoretical weak value curves (weak value of the diagonal polarization component in **a**; the weak value of the spatial projection operator in **b**). The determination of the theoretical uncertainty bands (the blue-shaded regions) is given in the Methods section. The pointer shifts and the error bars are calculated using the raw data from the experiment, denoted by red dots and bars.

formulated more precisely, and revealing its full conceptual import could be a stimulating line of future study.

## Methods

### Experimental architecture

**Setting up the Mach-Zehnder interferometer.** The schematic of the experimental setup is given in Fig. 5. The stream of single photons of wavelength 810 nm (bandwidth  $\sim 2$  nm) are made incident on the MZI from a polarization-maintaining single-mode fiber PMSMF<sub>2</sub> [PM780-HP, Thorlabs] to minimize pointing fluctuations of the beam. A suitable collimating lens COL [F240FC-780, Thorlabs] is used to get a beam size of  $\sim 1.5$  mm and minimize divergence. The beam is passed through a Glan-Thompson polarizer GT [GTH5-B, Thorlabs] to ensure the polarization is horizontal with a high degree of purity before entering the 50:50 beam splitter  $BS_1$  [BS014, Thorlabs].

In order to ensure that the path difference between the two arms of the MZI is negligible compared to the coherence length of the stream of detected photons, we use a corner cube retroreflector CCR [PS976M-B, Thorlabs] mounted on an actuator [ZST225-B, Thorlabs] attached to a 3D translation stage in one of the arms (here in the arm B). The actuator is adjusted so that the path difference is ensured to be within  $\sim 2$  microns. The CCR is used instead of a mirror assembly to avoid angular beam deviation upon translation. The CCR is attached to a piezo (osi-stack) which is used to stabilize the phase difference between the two arms of the MZI described later. However, since the CCR itself creates an additional path difference, this is macroscopically compensated using the three mirrors  $M_{T_1}$ ,  $M_{T_2}$  and  $M_{T_3}$  [NIR 5102, Newport] in the A arm of the MZI. The CCR, however, introduces ellipticity in the polarization of the beam in arm B. This is corrected using a half-wave plate  $HWP_c$  [WPA03-H-810, Newlight Photonics] followed by quarter-wave plate  $QWP_c$  [WPA03-Q-810, Newlight Photonics] and the polarization is made vertical. An additional polarizing beam splitter  $PBS_T$  is introduced after the three mirrors in arm A to further purify the polarization.

The second beam splitter  $BS_2$  [BS014, Thorlabs] is fixed at the intersection point of the two beams and oriented to roughly ensure the collinearity of the MZI. For fine alignment, the tip-tilt degrees of freedom of the mirror mounts are used to ensure collinearity, and the overlap of the beams is ensured by the translation of the CCR. The overlap of beams is ensured down to 5 microns (although the precision of measuring the center is much higher, at 0.1 microns, the spatial noise in the beam limits the accuracy) and the angle between the two beams emerging out of the second beam splitter ( $BS_2$ ) is ensured to be less than  $10^{-5}$  radians (the actual value may be  $\sim 10^{-7}$  radians as estimated from the fringe stability of the interferometer). A half-wave plate  $HWP_{post}$  [WPZ0-200-L/2-810, Castech] mounted in a motorized rotation mount [PRM1/MZ8, Thorlabs] is placed before a polarizing beam splitter ( $PBS_{post}$ ) at one of the exit ports of the second beam splitter ( $BS_2$ ). The post-selected state changes with the change in the angle of  $HWP_{post}$ . In addition to the angle of interest (i.e., when the fast axis of the  $HWP_{post}$  is aligned along the horizontal), two more post-selection angles are chosen to measure the reference pointer positions associated with the eigenvalues 0 and 1, respectively.

This enables evaluating the weak value for a particular post selection from the measured pointer shift.

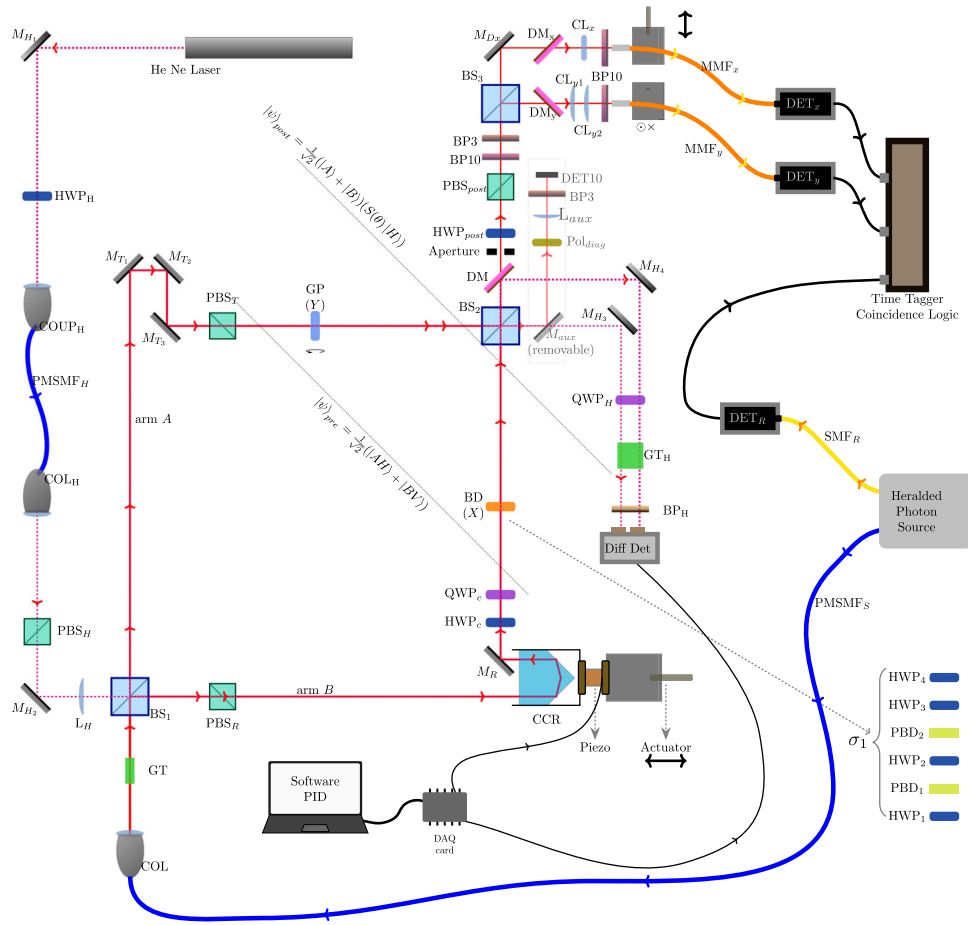
**Pre- and post-selection.** The pre-selected state is prepared after the compensating wave plate  $QWP_c$  on arm B and after  $PBS_T$  in arm A as depicted in Fig. 5. The post-selected state is obtained by back-evolving the transmitted component of the post-selection PBS ( $PBS_{post}$ ) to a time before the second beam splitter  $BS_2$  of the MZI. Such a state, which is thus guaranteed to be transmitted in the  $PBS_{post}$ , is given by

$$|\phi(\theta)\rangle = \frac{1}{\sqrt{2}}(|A\rangle + |B\rangle) \otimes S(\theta)|H\rangle \quad (1)$$

Here  $S(\theta)$  is the Jones matrix for the HWP whose fast axis is orientated at an angle  $\theta$  from the horizontal in the post-selection.

**Ensuring coherence.** A bandpass filter BP10 [FB810-10] followed by another BP3 [LL01-810-25] are used after  $PBS_{post}$  to prevent the light of other wavelengths from being detected and also to narrow the linewidth down to at most 3 nm. The bandwidth of the filter determines the minimum coherence length. Visibility of the interference upon a suitable (diagonal, at  $\theta = 22.5^\circ$ ) polarization post-selection is measured as a function of the path length difference by moving the actuator (in small steps) on which the CCR is mounted. Finally, the actuator is left at the position where maximum visibility is obtained.

**Phase stabilization.** The relative phase between the two arms of the interferometer can drift due to mechanical and acoustic vibrations and therefore the CCR needs to be moved accordingly in order to maintain a constant phase relationship between the two arms. This is achieved by using the piezo (attached to the CCR) which contracts or expands depending on the voltage provided to it, thus causing the CCR to move. For this, a PID algorithm is implemented on a computer along with a DAQ card [USB-6003] which is used to generate and receive voltages. The phase shift in the interferometer is monitored by measuring the difference in power in the two output ports of the second beam splitter  $BS_2$  for a Helium-Neon laser (He Ne) beam of wavelength 633 nm, inserted into the MZI from the other input port of the first beam splitter ( $BS_1$ ). This beam is mostly blocked by the Dichroic Mirror  $DM$  [DMLP735, Thorlabs] placed after  $BS_2$  in addition to the bandpass filters (BP10 and BP3). Before the differential detector (Diff Det), the polarizations of the He Ne beams coming from two output ports of  $BS_2$  are transformed into a circular basis using quarter-wave plate  $QWP_H$  and then projected to horizontal polarization using  $GT_H$  to achieve maximum visibility. The differential intensity signal obtained from the 633 nm beam is calibrated with the intensity of the 810 nm laser measured at the other output port (at which the post-selection is not performed) of  $BS_2$  with diagonal polarization projection using a polarizer and a photodetector [DET10/M, Thorlabs] as a function of voltage given to the piezoelectric transducer. When the path difference is within one wavelength, these two signals become almost linear enabling the usage of the differential intensity signal to stabilize the phase difference within low uncertainty.



**Fig. 5 Experimental setup of the complete Mach-Zehnder interferometer.** Phase stabilization is implemented using a Helium-Neon laser (He-Ne) beam of wavelength 633 nm, a corner cube retroreflector (CCR), PID programs in LabView, data acquisition (DAQ) card, and a differential detector (Diff Det). The dotted lines drawn diagonally, represent pre- and post-selection stages. In other components, PBS, BS, GT, M, DM, HWP, QWP, BP, BD, GP, MMF, SMF, PMSMF, CL, COUP, and COL stands for polarizing beam splitter, beam splitter, Glan-Thompson polarizer, mirror, dichroic mirror, half-wave plate, quarter-wave plate, bandpass filter, beam displacer, glass plate, multi-mode fiber, polarization-maintaining multi-mode fiber, single-mode fiber, polarization-maintaining single-mode fiber, cylindrical lens, coupler, and collimator, respectively.

*Weakly coupling the spatial DOF using a tilted glass plate.* A parallel window GP [WG41010-B, Thorlabs] is placed in arm A and is tilted to cause a vertical shift of ~50 microns in the beam. Tuning the angle of tilt of the glass plate, the shift in the beam can be controlled. If the shift were more than the beam width of 1.9 mm, observing this shift after the post-selection would have indicated whether the photon came from arm A or arm B. The shift of ~50 microns being much less than the beam width ensures that the observable ( $\hat{Y}_A$ ) is weakly coupled. The interaction Hamiltonian that couples the transverse spatial profile of the beam (pointer) with the observable in path A can be expressed as,

$$\hat{H}_A = g_A(t)\hat{Y}_A \otimes \hat{P}_y = g_A(t)(\hat{\Pi}_A \otimes \hat{1}) \otimes \hat{P}_y \quad (2)$$

where  $\int_0^{t_A} g_A(t)dt = g_A$  is the interaction strength that depends on the thickness and the tilt of the glass plate ( $t_A$  being the interaction time with the glass plate).  $\hat{\Pi}_A$  is the path projector operator associated with path A of the interferometer and  $\hat{P}_y$  is the momentum operator conjugate to the pointer variable  $y$ .

*Weakly coupling the diagonal component of polarization DOF using a composite beam displacer.* A polarizing beam displacer (PBD) allows the ordinary component of polarization of the beam incident on it to pass through without any deviation and causes a lateral shift (depending upon its thickness) in the path of the extraordinary component of polarization of the incident beam. Thus, the operation of a PBD can be considered as  $\sigma_3$  measurement operation. The  $\sigma_1$  measurement operator can be constructed from the  $\sigma_3$  measurement operation. Here the  $\sigma_3$  measurement operator is created using two beam displacers  $PBD_1$  and  $PBD_2$  [PDC 12005, Newlight Photonics] oriented in such a way that one of them causes ~50 microns shift in the extraordinary component along one direction (say +X) and the other shifts the extraordinary component by ~50 microns in the opposite direction (-X) horizontally. A half-wave plate  $HWP_2$  (fast axis at  $\pi/4$ ) is inserted between the two beam displacers so that the extraordinary beam for the first PBD

becomes the ordinary component for the second PBD and vice versa. This is followed by another half-wave plate  $HWP_3$  (with fast axis at  $\pi/4$ ) so that the ordinary and the extraordinary polarized beams have the same phase in the description of the  $\sigma_3$  operator. The whole  $\sigma_3$  measurement operator is placed between two half-wave plates  $HWP_1$  and  $HWP_4$  [WPA03-H-810] with their fast axes oriented at angle  $\pi/8$  to realize the  $\sigma_1$  operator.

The overall evolution operator associated with all the optical components is,

$$\mathcal{O} = \left(1 \otimes S\left(\frac{\pi}{8}\right)\right) \left(1 \otimes S\left(\frac{\pi}{4}\right)\right) U_{-X}^{BD} \left(1 \otimes S\left(\frac{\pi}{4}\right)\right) U_{+X}^{BD} \left(1 \otimes S\left(\frac{\pi}{8}\right)\right) \quad (3)$$

where  $S(\theta)$  is the Jones matrix of a HWP whose fast axis is oriented at an angle  $\theta$  with respect to the horizontal;  $S(\theta) = \cos(2\theta)\sigma_z + \sin(2\theta)\sigma_x$  and  $U_{\pm X}^{BD}$  is the operator associated with the PBD whose optic axis is oriented in a way that causes a lateral shift to the extraordinary component of the beam along the  $\pm X$  direction. In this experiment both the PBDs are aligned in a way that acts on the beam with transverse profile  $g(x, y)$  as,

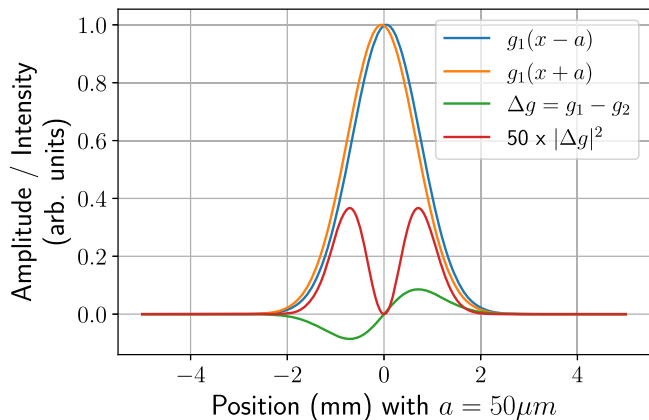
$$g(x, y) \otimes (\alpha|H\rangle + \beta|V\rangle) \xrightarrow{U_{\pm X}^{BD}} g(x, y) \otimes \alpha|H\rangle + g(x \pm X) \otimes \beta|V\rangle \quad (4)$$

The evolution operator  $\mathcal{O}$  can be considered close to a unitary operator up to the separation of the beams.

The interaction Hamiltonian that couples the pointer, i.e., the transverse spatial profile of the beam with the  $\sigma_1$  polarization operator in path B can be expressed as,

$$\hat{H}_B = g_B(t)\hat{X}_B \otimes \hat{P}_x = g_B(t)(\hat{\Pi}_B \otimes \hat{\sigma}_1) \otimes \hat{P}_x \quad (5)$$

where  $\int_0^{t_B} g_B(t)dt = g_B$  is the interaction strength that depends on the length of the crystal, the refractive indices of the material associated with e-ray and o-ray, the angle of incidence etc ( $t_B$  being the interaction time with the optical components corresponding to  $\sigma_1$  operator).  $\hat{\Pi}_B$  is the path projector operator associated with path B of the interferometer and  $\hat{P}_x$  is the momentum operator conjugate to the pointer variable  $x$ .



**Fig. 6 Beam alignment procedure.** Destructive Interference intensity pattern (shown after multiplication by 50 in red) is obtained when two Gaussians  $g_1$  and  $g_2$  are displaced in opposite directions by the displacement  $a$ . The centroid of this interference pattern has more errors due to the presence of noise. The centroid of the pattern is also very sensitive to the phase difference between the two Gaussian beams.

*Alignment procedure for joint observation.* Ideally, the zero reference of the beam, on a 2D plane after the post-selection would be at the position where both the beams from arm A and arm B merge. They are expected to be overlapping and collinear at the detection plane. However, when components for the weak interaction with the  $\sigma_1$  polarization component are inserted in arm B, the beam displacers ( $PBD_1$  and  $PBD_2$ ) need to be tilted in order to adjust the phase shift between the emergent e-ray and o-ray so that in the limit of the beam displacement between them going to zero, the evolution operator due to the interaction remains identity. Due to the tilt as well as a slight angular deviation of the beam from the components, the beam in arm B gets refracted after the components are inserted. This causes a slight non-collinearity and translation of the beam. The change in collinearity is very small and can be adjusted by maximizing the visibility when post-selection is either diagonal or anti-diagonal. This is achieved by the tip/tilt of the mirror  $M_R$ . The displacement between the diagonal and anti-diagonal components is fixed by the alignment of components ( $PBD_1$  and  $PBD_2$ ) for the  $\sigma_1$  interaction. However, they should ideally be on either side, equidistant from the center of the beam emerging from arm A. One way to verify this would be to measure the beam center position from arm A with arm B blocked and vice versa. However, when arm A is blocked, the pre-selected polarization in arm B is orthogonal to the post-selected polarization. Due to the displacement between diagonal and anti-diagonal components, we have the destructive interference pattern after post-selection as shown in Fig. 6.

The centroid of the destructive interference pattern tends to be error-prone. Therefore, utilizing the fact that the centers of the beams in arms A and arm B coincide, one needs to use the resultant interference pattern formed when the post-selection is diagonal and anti-diagonal. From theory, these two displacements need to be symmetric about the center of the beam of arm A. This is achieved by translating the CCR and measuring the resultant centroid at three post-selection configurations. Once the above alignment is ensured, the glass plate in arm A which was back aligned, is now tilted so that it causes the desired shift along the vertical direction when arm B is blocked. All the above steps are performed with a pulsed laser source and data is acquired with a beam profiler. The 2D centroid of the beam is scaled to the weak value. The scaling can be achieved by subtracting the ensured zero position as mentioned earlier and scaling it with the pointer shift corresponding to the eigenvalues with individual arms blocked. This can be done with beam profiler data as blocking and insertion of components are all performed with beam profiler as the monitoring tool for the pulsed laser source. However, once the measuring device is changed, the information about the absolute position in different configurations is lost. The beam profiler is then taken out of the setup and the multimode fibers mounted on a translation stage are used. The weak value is measured at the three post-selection angles to ensure that the alignment of multimode fibers is consistent with the beam profiler data. Once the above is ensured, the pulsed laser beam is replaced with a stream of single photons coming from a single photon source to measure singles and coincidences. Here, we scale the pointer shift to weak values by subtracting the pointer shift at post-selection HWP angle  $45^\circ$  (corresponding to the zero weak value). Similarly, displacement by weak value 1 happens when post-selection HWP angle is  $90^\circ$ .

#### Data acquisition and analysis

*Methods for acquiring data.* In order to subsequently use a single photon source, first a 100 fs pulsed laser [Mira 900 D Ti:Sapphire, rep rate: 76 MHz] is used with an average power of  $\sim 2$  mW to ensure good alignment. Although the coherence

length of the pulsed laser ( $\approx 60 \mu\text{m}$ ) is lower (compared to continuous wave), it is slightly enhanced by the use of the bandpass filter ( $\approx 218 \mu\text{m}$  with 3 nm bandpass filter for the central wavelength of 810 nm) so that the pulsed laser has almost the same central wavelength and the bandwidth as the single photon source to be used later. A beam profiler [Dataray UCD -15] is placed after the bandpass filter. The post-selection HWP angle is rotated to the angle  $67.5^\circ$  which creates the destructive interference profile along the diagonal. The phase difference is adjusted to make this destructive interference pattern as symmetric as possible along the diagonal. The slight spatial noise in the beam profile i.e., deviation from a perfect Gaussian profile typically would dominate the destructive interference pattern. The overall power incident on the beam profiler also reaches the minimum which is another indicator of the correct phase difference to which the Mach-Zehnder interferometer is locked. The post-selection HWP is rotated and post-selections are varied by choosing different HWP angles. Five images are captured for each HWP angle i.e., for each post-selection. The first-order centroid of the 2D images is computed. The pointer shifts are scaled to the weak value using the pointer shifts at the post-selection HWP angles  $45^\circ$  and  $90^\circ$  as reference.

For the single-photon source, the timing information along with the spatial profile needs to be measured. The timing information ensures that the contribution of multi-photon events to the pointer shift is negligible. For this SPAD detectors [Tau SPAD-20, Pico quant] are used. The photons are collected using a bare multimode fiber [M42L02, Thorlabs] with a core diameter of 50 microns. The fibers  $MMF_x$  and  $MMF_y$  are moved in steps of 50 microns to sample the Gaussian profile along the horizontal and vertical directions, respectively. A width of about 3 mm across the beam is covered with 61 points. Although the use of such fibers averages the intensity over 50 microns, the precision with the centroid is much better than this and depends on the total number of photons collected. To enhance the collection, a (combination of) cylindrical lens ( $CL_x$ ,  $CL_{y_1}$  and  $CL_{y_2}$ ) is used to compress one spatial dimension. The multi-mode fiber tip is placed at the focus of the cylindrical lens and is translated to obtain the spatial profile.

Since the objective is to jointly observe the two pointers, a 50:50 beam splitter  $BS_3$  [BS014] is used to divide the beam. One beam is used to reconstruct the horizontal profile (X) and the other beam is used to reconstruct the vertical profile (Y). Since the beam splitter sends the photon towards the horizontal or the vertical detector with inherent randomness and there is no change of experimental settings within the interferometer (i.e., between pre- and post-selection), the horizontal and vertical centers of the beam are jointly obtained for the ensemble of photons for a given post-selected state.

The simultaneous determination of pointer shifts could also be done using a camera which can give both information about the  $x$  and  $y$  positions of the center of the beam from a single detection. However, it is required to gate the camera with  $\sim 1-5$  ns precision to select only the heralded photons from the SPDC process, so that detection with single photons is ensured. But due to the unavailability of the commensurate camera with appropriate gating precision, we chose the method discussed above which is equivalent in terms of its purpose.

*Statistics and error analysis.* For a particular post-selection, the Gaussian profiles of the beam along the horizontal and vertical directions are reconstructed by collecting the photons (in  $MMF_x$  and  $MMF_y$ ) from 61 different points (separated by  $50 \mu\text{m}$ ) along the beam width.

For the post-selection  $|\phi(0^\circ)\rangle$  i.e., when the post-selection HWP angle is set to  $0^\circ$ , 16 coincidence readings per position of the MMF are taken. Any one of these 16 readings at a particular position is chosen randomly and it is repeated for all 61 positions to construct a Gaussian profile. Thus  $16^{61}$  such possible profiles can be constructed from the collected data. This method of preparing a large number of data sets by resampling from the original dataset is called statistical bootstrapping<sup>28,29</sup>. Out of that,  $10^4$  such Gaussian profiles are sampled and each such profile is fitted with a Gaussian function to determine the center. This gives the distribution of the position of the pointer (say  $X$ ) for that post-selected state  $|\phi(0^\circ)\rangle$ .

For the post-selection angle  $45^\circ$ , i.e., for  $|\phi(45^\circ)\rangle$ , three coincidence readings are taken for each position of the MMF (for a total of 61 positions). The Gaussians are reconstructed by randomly choosing any of the three readings from the dataset recorded per position, amounting to a total of  $3^{61}$  possible profiles from which  $10^4$  profiles are sampled and centers are determined from Gaussian function fittings. Let us call the distribution of centers when the post-selection angle is  $45^\circ$  as  $X_0$ .

Similarly, for the post-selection angle,  $90^\circ$ , 3 coincidence readings per MMF position for a total of 61 positions are recorded. The corresponding distribution of the beam for the post-selected state  $|\phi(90^\circ)\rangle$  is considered to be  $X_1$ , which again is obtained from Gaussian fits of  $10^4$  profiles sampled out of  $3^{61}$  possible profiles. Likewise, for the other post-selection angles, a minimum of three coincidence readings per position of the MMF are taken for a total of 61 such positions. This leads to a minimum of  $3^{61}$  profiles, out of which  $10^4$  profiles are sampled out to generate the distribution of  $X$  and  $Y$  weak values.

We note that we are sampling  $10^4$  profiles for all post-selection angles considered. The post-selected state  $|\phi(0^\circ)\rangle$  is our state of interest for the demonstration of the Partial Cheshire Cat phenomenon. The mean and standard deviation of the weak values of the path-projector in one arm (here  $\hat{Y}_A = \hat{\Pi}_A \otimes \hat{1}$ ) and the component of polarization d.o.f. in the other arm (here  $\hat{X}_B = \hat{\Pi}_B \otimes \hat{\sigma}_1$ ) needs to be determined experimentally from the observed pointer shifts for post-selected state  $|\phi(0^\circ)\rangle$  and scaling them with respect to the one unit of weak value as



computed from the difference between the experimentally obtained pointer shifts at two reference post-selected states,  $|\phi(90^\circ)\rangle$  and  $|\phi(45^\circ)\rangle$ , corresponding to weak values 1 and 0 respectively. In order to be able to comment on the experimental mean and  $1\sigma$  error for  $X^w$  and  $Y^w$  ideally, we need to collect sufficient statistics for each post-selection angle, with the condition that all the data has to be taken for the same alignment of the setup while maintaining the constant phase relationship between the two arms. This led to our choice of taking more initial statistics at the desired point. However, ultimately, we have used the same number of Gaussian profiles for all three post-selection points. Since the profiles are drawn at random, we can create the distribution of weak values by computing,

$$X^w = \frac{X - X_0}{\langle X_1 - X_0 \rangle} \tag{6}$$

The statistical random errors are represented by a standard deviation of  $X^w$ . The above distribution is computed for both horizontal pointer shift and vertical pointer shift associated with the interaction of  $\hat{X}_B$  and  $\hat{Y}_A$  respectively. The random errors come from the numerator since we have taken the expectation value in the denominator. The beam has a certain drift over time, thus it may happen that while reconstructing the Gaussian profiles from the samples chosen randomly out of three possibilities for each position of the MMF, few values of  $X_0$  could be very close to few values of  $X_1$ . Hence to avoid spurious weak values for the cases when the value in the denominator turns out to be zero by chance, we have chosen the statistical mean of  $\langle X_1 - X_0 \rangle$  which will give the average value of the scaling factor needed to compute the weak values from the pointer shifts.

To further motivate the importance of statistical bootstrapping, we acquired coincidence data for post-selection angles other than  $|\phi(0^\circ)\rangle$ . As discussed before, we took maximum statistics for the  $|\phi(0^\circ)\rangle$  point but also collected enough statistics at some other post-selection angles.

As discussed above, we had to complete the whole experiment within a certain time frame due to the unavoidable beam drift from the source that could have affected the pointer shifts being observed as the experiment progressed. Hence, fewer coincidence readings were taken for points other than the point of interest. It was ensured that all data acquisition happened with the same experimental settings and stabilization conditions. Using the raw data from these measurements, the mean and  $1\sigma$  error for the weak values corresponding to all the different post-selected states are calculated and presented in Fig. 4 of the main text.

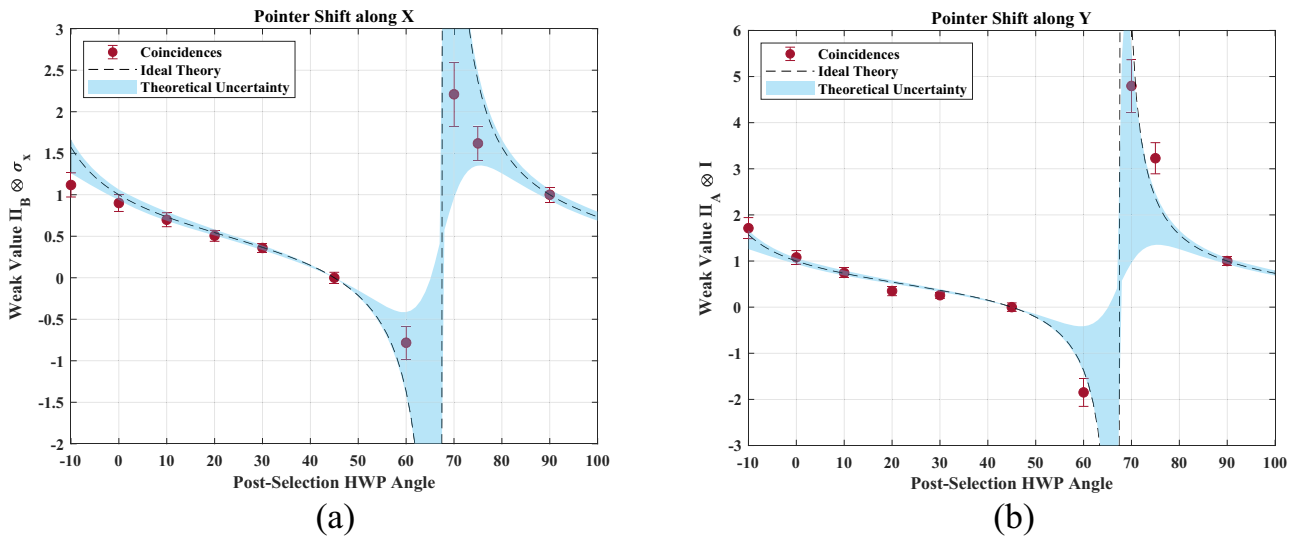
The resampling of the raw data for all the different post-selection angles was done in the same way as discussed earlier in this section. From the measured data,  $10^4$  profiles are sampled for every post-selection angle, and centers are determined from Gaussian function fittings. The same number of samplings at all post-selection angles was done to remove any bias in the resampling of the coincidences and generation of random Gaussian profiles. With the centers determined, the distribution of pointer variables was obtained, and using the equation (6) from earlier in this section for weak value computation, the weak values in X and Y were generated. The mean and  $1\sigma$  error for the weak values calculated using the bootstrap analysis corresponding to the different post-selected states are plotted in Methods Fig. 7a, b.

In the plots, the ideal theory curve and corresponding error band are both plotted. For the theoretical curve generation, as our pre-selected state, we consider the state  $|\psi\rangle = \frac{1}{\sqrt{2}}(|A\rangle|H\rangle + |B\rangle|V\rangle)$ , where  $|A\rangle$  and  $|B\rangle$  denote the spatial wavefunctions in arms A and B respectively. Here we assume the interferometer has zero path difference. The post selected state is given by  $|\phi(\theta)\rangle = \frac{1}{\sqrt{2}}(|A\rangle + |B\rangle) \otimes S(\theta)|H\rangle$ .  $S(\theta)$  is the Jones matrix for post-selection HWP. Using the expression in section 2.1 of supplementary Note 2 for weak value calculation and the pre-and post-selected states discussed above, we calculated weak values for the spatial projection operator by varying the post-selection angle.

The theory plot thus generated is for ideal conditions, but while performing the experiment, the interferometer may incur a slight path difference between the two arms, which in turn results in phase instabilities. The path difference changes the pre-selected state by adding a phase component. Taking this non-idealness into account, a range of phase angles was chosen, which corresponds to different set points during the stabilization of the interferometer. While phase-locking the interferometer, we choose certain setpoints where the interferometer can be kept phase locked during the entire run time of the experiment, which is done using the differential detector taking into account the difference between intensities of the HeNe laser beam from both output arms that represents the relative phase between them as a Cosine function. The set points are chosen from the slope of the function where the interferometer was found to be very stable. Using the range of phase angles in the pre-selected state, the maximum and minimum possible weak values were calculated as a function of the post-selection angle, which gave rise to the generation of the theory band.

The experimental results were found to be matching with the expectations from the theory. With bootstrap analysis, the errors are also found to lie well within the theory band.

From the values in Tables 1 and 2, it is clear that we converge on the  $1\sigma$  error value more accurately using statistical bootstrapping than the raw analysis of the



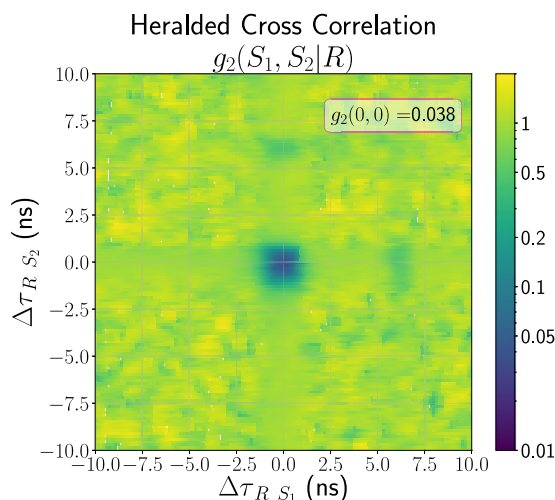
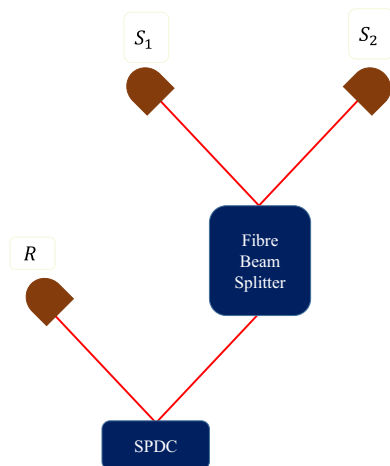
**Fig. 7 Weak values with data resampling.** **a** Pointer shift (detected in coincidence with the heralded photon) along X as a function of post-selection angle with  $1\sigma$  error bar, **b** Pointer shift along Y as a function of post-selection angle with  $1\sigma$  error bar. The black dashed line in each plot represents the theoretical weak value curve (the weak value of the diagonal polarization component in **a**, the spatial projector weak value in **b**). The blue-shaded regions indicate the theoretical uncertainty band. The pointer shifts and the error bars are calculated by resampling the data and generating  $10^4$  Gaussian profiles corresponding to each post-selection angle (statistical bootstrapping).

**Table 1  $1\sigma$ s of  $X^w$ s with and without bootstrap.**

Post-selection angle	-10°	0°	10°	20°	30°	45°	60°	70°	85°	90°
$1\sigma$ Without Bootstrap	0.249	0.183	0.132	0.105	0.084	0.103	0.420	0.291	0.279	0.190
$1\sigma$ With Bootstrap	0.144	0.102	0.083	0.067	0.050	0.066	0.199	0.387	0.209	0.089

**Table 2**  $1\sigma$ s of  $Y^w$ s with and without bootstrap.

Post-selection angle	$-10^\circ$	$0^\circ$	$10^\circ$	$20^\circ$	$30^\circ$	$45^\circ$	$60^\circ$	$70^\circ$	$85^\circ$	$90^\circ$
$1\sigma$ without bootstrap	0.607	0.375	0.231	0.324	0.131	0.174	0.372	0.858	0.594	0.268
$1\sigma$ with bootstrap	0.229	0.146	0.108	0.102	0.069	0.092	0.303	0.567	0.337	0.101



**Fig. 8** Heralded cross-correlation function. Heralded cross-correlation is performed with source pump power 20 mW and coincidence time window 312.5 ps, to verify the single-photon nature of the heralded photons generated from spontaneous parametric down-conversion (SPDC) source. The plot on the right-hand side shows a  $g_2$  value of 0.038.

measured data. Hence using bootstrap analysis, a better approximation of the central limit theorem can be achieved. During the analysis, it was observed that as we approached a sampling number of  $10^3$ , we were already closing in on the  $1\sigma$  error.  $10^4$  number of samples in this particular analysis can be regarded as more than sufficient and is thus used for obtaining an accurate error bar from the experiment. Also, it can be seen that around the amplification point, which is happening at a  $67.5^\circ$  post-selection angle, the bootstrap analysis is not leading to much of an improvement, and the  $1\sigma$  error remains larger for the X weak value while there is a marginal improvement in the Y weak value with bootstrap. That may be mainly attributed to the following reasoning. The experiment, like any other weak measurement-based experiment, is highly error-prone at the amplification point. In order to address this, ideally we should have measured a lot of statistics at the amplification zone. However, we could measure a small number of mother data sets because of the experimental time constraints and this may not have been sufficient to act as a seed to the large data pool that is further generated using the bootstrap method. However, as discussed earlier, our focus in this experiment was to measure the weak values for the post-selected state  $|\phi(0^\circ)\rangle$  and we have measured at few other post-selection points to demonstrate that our theory matches with experiment beyond the point of interest and also to illustrate the merit of our statistical bootstrap based error analysis.

On measuring a few profiles at a particular post-selection angle and then changing the post-selection angle to observe a certain shift, it could so happen that the observed shift is more or less than expected due to drift in the position of the beam over time. This drift typically arises from the effect of temperature, pressure, and humidity on optomechanics and fibers (mainly PMSMF). The exact beam drift can not be monitored during the experiment and can only be estimated. The beam drift is estimated in a separate experiment where the transverse profile of the beam in arm A (with arm B blocked) is repeatedly measured with the moving MMF for a long period. The drift in centroid would represent the drift of the beam's center over time. The standard deviation of the centers as obtained from the repeated scans over the beam from path A is  $8.4\ \mu\text{m}$  and  $10.4\ \mu\text{m}$  for coincidences along X and Y, respectively. The standard deviation of the centroid over time indicates the range of the systematic error, which changes the unit scale of the weak value.

**Single-photon source characteristics.** The experiment uses a heralded single photon source generated using spontaneous parametric down-conversion of 405 nm pump beam in a type-II PPKTP crystal in a collinear Sagnac geometry. As shown in Fig. 5 one stream of photons (signal photons) is made incident on the MZI using a PMSMF<sub>S</sub>. Although the source is bright and the singles count rate is in the MHz domain, photons with rates in the kHz domain are detected with the multi-mode fibers (MMF<sub>x</sub>, MMF<sub>y</sub>) shown in Fig. 5 due to the collection area of the fibers. Each stream of photons (singles) is known to have Poissonian statistics and only the

heralded photons (coincidences) follow sub-Poissonian statistics. The heralded cross-correlation function is defined for the SPDC process as

$$g_2(\Delta\tau_1, \Delta\tau_2) = \frac{N(R)C(S_1(\Delta\tau_1), S_2(\Delta\tau_2)|R)}{C(S_1(\Delta\tau_1)|R)C(S_2(\Delta\tau_2)|R)}. \quad (7)$$

Here,  $N(R)$  is the number of photons in the reference (R) detector  $DET_R$  in a given time duration (see Fig. 8).  $C(S_1(\Delta\tau_1), S_2(\Delta\tau_2)|R)$  refers to the triple coincidences when  $S_1$  is delayed by  $\Delta\tau_1 (= \Delta\tau_{RS_1})$  and  $S_2$  is delayed by  $\Delta\tau_2 (= \Delta\tau_{RS_2})$  with respect to R. The coincidences between R with  $S_1$  delayed by  $\Delta\tau_1$  and between R with  $S_2$  delayed by  $\Delta\tau_2$  is denoted by  $C(S_1(\Delta\tau_1)|R)$  and  $C(S_2(\Delta\tau_2)|R)$  respectively.

The  $g_2(0, 0)$  is  $\sim 0.038$  thus implying that the stream of photons from  $S_1$  or  $S_2$  when heralded with R shows single-photon characteristics.

### Data availability

The data supporting this work are available from the corresponding author upon reasonable request.

Received: 18 April 2023; Accepted: 21 July 2023;

Published online: 07 August 2023

### References

1. Wheeler, J. A., & Zurek, W.H. Quantum theory and measurement. *Princeton University Press*, Princeton, pp. 182–200 (1983).
2. V, J. et al. Experimental realization of Wheeler's delayed-choice gedanken experiment. *Science* **315**, 966–968 (2007).
3. Aharonov, Y., Albert, D. Z. & Vaidman, L. How the result of a measurement of a component of the spin of a spin-1/2 particle can turn out to be 100. *Phys. Rev. Lett.* **60**, 1351 (1988).
4. Aharonov, Y., Popescu, S., Rohrlich, D. & Skrzypczyk, P. Quantum cheshire cats. *N. J. Phys.* **15**, 113015 (2013).
5. Denkmayr, T. et al. Observation of a quantum cheshire cat in a matter-wave interferometer experiment. *Nat. Commun.* **5**, 4492 (2014).
6. Atherton, D. P., Ranjit, G., Geraci, A. A. & Weinstein, J. D. Observation of a classical Cheshire cat in an optical interferometer. *Opt. Lett.* **40**, 879–881 (2015).
7. Ashby, J. M., Schwarz, P. D. & Schlosshauer, M. Observation of the quantum paradox of separation of a single photon from one of its properties. *Phys. Rev. A* **94**, 012102 (2016).

8. Kim, Y. et al. Observing the quantum Cheshire cat effect with noninvasive weak measurement. *npj Quantum Inf.* **7**, 13 (2021).
9. Duprey, Q., Kanjilal, S., Sinha, U., Home, D. & Matzkin, A. The quantum cheshire cat effect: theoretical basis and observational implications. *Ann. Phys.* **391**, 1–15 (2018).
10. Aharonov, Y., Bergmann, P. G. & Lebowitz, J. L. Time symmetry in the quantum process of measurement. *Phys. Rev.* **134**, B1410 (1964).
11. George, R. E. et al. Opening up three quantum boxes causes classically undetectable wavefunction collapse. *Proc. Natl Acad. Sci.* **110**, 3777–3781 (2013).
12. Bohr, N. On the notions of causality and complementarity. *Dialectica* **2**, 312–319 (1948).
13. Wheeler, J. A. How come the quantum? *Ann. N. Y. Acad. Sci.* **480**, 304–331 (1986).
14. Pryde, G., O'Brien, J., White, A., Ralph, T. & Wiseman, H. Measurement of quantum weak values of photon polarization. *Phys. Rev. Lett.* **94**, 220405 (2005).
15. Hosten, O. & Kwiat, P. Observation of the spin hall effect of light via weak measurements. *Science* **319**, 787–790 (2008).
16. Kocsis, S. et al. Observing the average trajectories of single photons in a two-slit interferometer. *Science* **332**, 1170–1173 (2011).
17. Lundeen, J. et al. Direct measurement of the quantum wavefunction. *Nature* **474**, 188–191 (2011).
18. Nirala, G., Sahoo, S., Pati, A. & Sinha, U. Measuring average of non-Hermitian operator with weak value in a Mach-Zehnder interferometer. *Phys. Rev. A* **99**, 022111 (2019).
19. Ramos, R. et al. Measurement of the time spent by a tunnelling atom within the barrier region. *Nature* **583**, 529–532 (2020).
20. Pan, Y. et al. Weak-to-strong transition of quantum measurement in a trapped-ion system. *Nat. Phys.* **16**, 1206–1210 (2020).
21. Liu, Z. H. et al. Experimental exchange of grins between quantum Cheshire cats. *Nat. Commun.* **11**, 3006 (2020).
22. Piacentini, F. et al. Measuring incompatible observables by exploiting sequential weak values. *Phys. Rev. Lett.* **117**, 170402 (2016).
23. Martinez-Becerril, A. C. et al. Theory and experiment for resource-efficient joint weak-measurement. *Quantum* **5**, 599 (2021).
24. Sahoo, S. N., Home, D., Matzkin, A. & Sinha, U. Comment on “Observing the “quantum Cheshire cat” effect with noninvasive weak measurement” <https://arxiv.org/abs/2006.00792> (2020).
25. Margalit, Y. et al. Realization of a complete Stern-Gerlach interferometer: toward a test of quantum gravity. *Sci. Adv.* **7**, eabg2879 (2021).
26. Aharonov, Y., Cohen, E. & Popescu, S. A dynamical quantum cheshire cat effect and implications for counterfactual communication. *Nat. Commun.* **12**, 4770 (2021).
27. Schilpp, P. A. Albert Einstein; Philosopher, Scientist. *Philosophy* **26**, 363–365 (1951).
28. Efron, B. Bootstrap methods: another look at the Jackknife. *Ann. Stat.* **7**, 1–26 (1979).
29. Hesterberg, T.C., Moore, D.S., Monaghan, S., Clipson, A. & Epstein, R. Bootstrap methods and permutation tests. (eds. D. S. Moore and G. McCabe). *In: Introduction to the Practice of Statistics* (2nd ed.), New York: W.H. Freeman (2005).

## Acknowledgements

U.S. acknowledges partial support provided by the Ministry of Electronics and Information Technology (MeitY), Government of India under the grant for Center for Excellence in Quantum Technologies with Ref. No. 4(7)/2020 – ITEA and QuEST-DST project Q-97 of the Govt. of India. D.H. and U.S. would like to acknowledge partial support from the DST-ITPAR grant IMT/Italy/ITPAR-IV/QP/2018/G. DH also acknowledges support from the NASI Senior Scientist fellowship. We thank R. Chatterjee, S. Chatterjee, K. Joarder, Meena MS, and Hafsa Syed for technical assistance.

## Author contributions

S.N.S. and S.C. performed the experiment; S.N.S., S.C. and S.R.B. performed the data analysis; S.K. worked on the theoretical elements under the supervision of D.H. and A.M.; U.S., D.H. and A.M. conceived the experiment. The experiment was performed under the supervision of U.S. All authors contributed to the writing of the manuscript.

## Competing interests

The authors declare no competing interests.

## Additional information

**Supplementary information** The online version contains supplementary material available at <https://doi.org/10.1038/s42005-023-01317-7>.

**Correspondence** and requests for materials should be addressed to Urbasi Sinha.

**Peer review information** *Communications Physics* thanks the anonymous reviewers for their contribution to the peer review of this work.

**Reprints and permission information** is available at <http://www.nature.com/reprints>

**Publisher's note** Springer Nature remains neutral with regard to jurisdictional claims in published maps and institutional affiliations.



**Open Access** This article is licensed under a Creative Commons Attribution 4.0 International License, which permits use, sharing, adaptation, distribution and reproduction in any medium or format, as long as you give appropriate credit to the original author(s) and the source, provide a link to the Creative Commons license, and indicate if changes were made. The images or other third party material in this article are included in the article's Creative Commons license, unless indicated otherwise in a credit line to the material. If material is not included in the article's Creative Commons license and your intended use is not permitted by statutory regulation or exceeds the permitted use, you will need to obtain permission directly from the copyright holder. To view a copy of this license, visit <http://creativecommons.org/licenses/by/4.0/>.

© The Author(s) 2023